Geodesy and Geodynamics 14 (2023) 541–550

Contents lists available at ScienceDirect

Geodesy and Geodynamics

journal homepage: http://www.keaipublishing.com/geog

Synthetic aperture radar interferometry–based coseismic deformation and slip distribution of the 2022 Menyuan M_S6.9 earthquake in Qinghai, China

Qiang Zhao*, Fengyun Jiang, Liangyu Zhu, Jing Xu

The Second Monitoring and Application Center of China Earthquake Administration, Xi'an 713700, China

ARTICLE INFO

Article history:
Received 25 November 2022
Accepted 31 July 2023
Available online 6 September 2023

Keywords:
Geodesy
Coseismic deformation
InSAR technology
Inversion
Coulomb stress
Lenglongling fault
Fault movement
Menyuan earthquake

ABSTRACT

On January 8, 2022, a 6.9 magnitude earthquake occurred in Menyuan County, Qinghai Province, with the epicenter located at the intersection of the Tuolaishan Fault and the Lenglongling Fault, which are part of the Qilian–Haiyuan fault zone. This study investigated the sliding characteristics and seismic mechanism of the earthquake to understand the activity and seismic risk of the fault on the northeastern margin of the Qinghai–Tibet Plateau. This paper analyzed Sentinel-1 synthetic aperture radar images to obtain the coseismic deformation field of the earthquake, which was then used to invert the slip distribution of the seismogenic fault and the coseismic Coulomb stress on the surrounding faults caused by the earthquake. It was found that the earthquake was primarily characterized by sinistral strike-slip movement. Along the satellite line of sight, the south wall of the fault had a maximum deformation of 0.62 m, and the north wall had a maximum deformation of 0.48 m. The coseismic slip distribution results indicated that the maximum slip of the earthquake was 4.51 m, and the moment magnitude was M_W6.7. The Coulomb stress analysis showed that the 2016 Menyuan earthquake promoted the occurrence of the 2022 Menyuan earthquake.

1. Introduction

An M_S6.9 earthquake with a focal depth of 10 km occurred in Menyuan County (37.77 °N, 101.26 °E) in Haibei, Qinghai Province, at 1:45 a.m. (Beijing time), on January 8, 2022, according to the China Earthquake Networks Center website (https://news.ceic.ac.cn). The earthquake occurred in a remote area with high altitude, harsh geological and climatic conditions, and poor working and transportation conditions, 54 km from Menyuan County. After the earthquake occurred, different mechanisms provided various focal mechanism solutions (Table 1), indicating that the seismogenic fault of the earthquake was a high-dip strike-slip fault.

In terms of regional tectonics, this earthquake occurred at the intersection of the Lenglongling fault and the Tuolaishan fault in the middle of the Qilian Mountains (Fig. 1), which is part of the Qilian–Haiyuan fault, the most critical strike-slip fault system in the high northeastern margin of the Qinghai–Tibet Plateau. The Tuolaishan fault and the Lenglongling fault share a high number of sinistral strike-slip transport [1,2]. The Tuolaishan fault starts from Hala Lake in the west and ends at Liuhuanggoukou under Lenglongling in the east, with a general trend of NWW and a tendency of SW, totaling approximately 280 km in length. The fault is primarily sinistral strike-slip, with a late Quaternary sliding rate of 1–3 mm/yr in the western section and 4–6 mm/yr, in the eastern section, characterized by pronounced thrust properties [3,4]. The western section of the Lenglongling fault is connected to the Tuolaishan fault, and the eastern section is connected to the Jinqianghe fault. Its length is approximately 120 km, and the linear feature is relatively pronounced. Since the late Quaternary, the Lenglongling fault has been predominantly characterized by left-handed strike-slip movement with a thrust component ranging from 19 ± 5 mm/

Abbreviations: InSAR, synthetic aperture radar interferometry; LOS, line of sight.

* Corresponding author.
E-mail address: gke_1990@163.com (Q. Zhao).

Peer review under responsibility of Institute of Seismology, China Earthquake Administration.

Production and Hosting by Elsevier on behalf of KeAi

https://doi.org/10.1016/j.geog.2023.07.004

Table 1
Parameters of the focal mechanism solution of the January 8, 2022 Menyuan earthquake inverted by USGS and GCMT.

Information source	epicenter		focal depth (km)	strike (°)	dip angle (°)	angle of slip (°)	Magnitude (M_W)
	Lat (°)	Lon (°)					
USGS	37.828	101.290	11.5	104 13	88 75	15 178	6.6
GCMT	37.80	101.31	14.8	104 14	82 89	1 172	6.7

yr to 3.35–4.62 mm/yr [3,5–7]. Many researchers have used geodetic methods to study the current sliding rates of the Tuolaishan fault and the Lenglongling fault. Zheng et al. (2013) obtained the sliding rate for the Tuolaishan fault, which was approximately 4 mm/yr, using the GNSS velocity field from 1999 to 2007 [3]. Li et al. (2016) used the negative dislocation model to calculate the sliding rate and locking degree of the Qilian–Haiyuan fault and found that the sinistral strike-slip rate for the Tuolaishan section to the Lenglongling section gradually decreased from 5.5 mm/yr to approximately 4.5 mm/yr. Based on the block model [2], Li et al. (2018) calculated the slip rates of the faults in the northeastern margin of the Qinghai–Tibet Plateau [8]. The slip rates of the western section of the Tuolaishan section were approximately 2.9 mm/yr, while those of the eastern section were approximately 5.8 mm/yr. The slip rates of the Lenglongling fault–Jinqianghe Fault–Haiyuan fault were approximately 5.3 mm/yr. Synthetic aperture radar interferometry (InSAR) has been used to study the Haiyuan fracture in detail, and its sliding rate has been determined to be between 4.2 mm/yr and 11.5 mm/yr [2,9–11]. Overall, there is a considerable difference between the Quaternary slip rate of the Menyuan earthquake seismogenic fault and the current geodetic slip rate.

Historical seismic data has shown that earthquakes of magnitude 6 or higher near the epicenter of this earthquake include the 1986 Menyuan M_W6.0 earthquake, the 2016 Menyuan M_W5.9 earthquake, and the 1927 Gulang M_W7.7 earthquake [6,12–18]. In 1986 and 2016, two Menyuan earthquakes occurred on secondary faults on the north side of the Lenglongling fault [12,13,19–33]. Their focal mechanism solutions were low-dip thrust earthquakes, which were inconsistent with the left-lateral strike-slip nature of the Lenglongling fault [7,13]. The 1927 Gulang earthquake occurred on the Huangcheng–Shuangta fault, which is relatively far from the epicenter. Therefore, none of these earthquakes are characteristic seismic events for the Lenglongling fault. The strike-slip property of the 2022 Menyuan earthquake is consistent with the movement property of the Lenglongling–Tuoleshan fault, which is located at the intersection of these two strike-slip faults. Therefore, a detailed study of the fault movement in the 2022 Menyuan earthquake is crucial for understanding the north–northeast expansion of the Qinghai–Tibet Plateau.

Previous research on the interseismic deformation of the Tuolaishan–Lenglongling–Haiyuan fault has been undertaken using geological and traditional geodetic methods. However, the limitations of the distribution of monitoring stations and other factors make it challenging to obtain the fine regional surface deformation field using these methods. InSAR technology offers an advantage in obtaining high spatial resolution of surface deformation fields ranging from several meters to tens of meters. Furthermore, it does not require ground control points, making it a surface-type measurement mode. Currently, InSAR technology is widely used in the constraint of seismic fault parameters. However, most research on InSAR technology has predominantly focused on the Haiyuan fault, with relatively little research on the Tuolaishan–Lenglongling fault [9,11,34–36]. This earthquake is different from the 2021 Maduo M_S7.4 earthquake, the 2017 Jiuzhaigou M_S7.0 earthquake, and the 1986 and 2016 Menyuan earthquakes. All of these earthquakes have occurred on secondary faults. The seismogenic fault of this earthquake belongs to the main fault [4,6,7] and has pronounced sliding characteristics in the deformation field, which presents an excellent opportunity to study the characteristics of coseismic fault motion using high density deformation data.

After the earthquake, many scholars used InSAR technology and Sentinel-1 satellite images to obtain the coseismic deformation field of the earthquake, and the results showed that the maximum

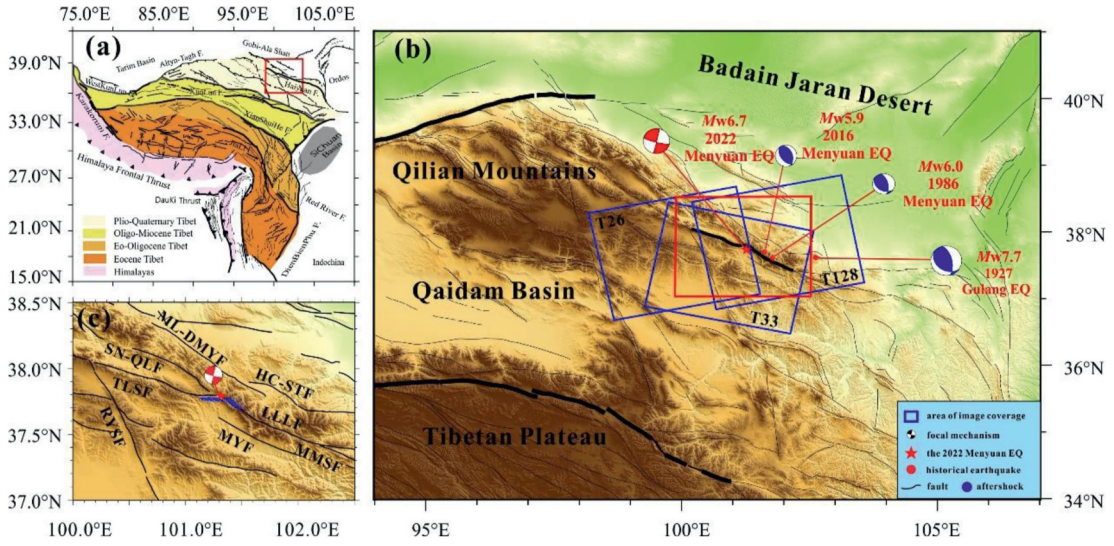

Fig. 1. Geological tectonic background of the 2022 Menyuan earthquake. (b) is the red box shown in (a), (c) is the red box shown in (b).

shape variable in the LOS direction was 0.60–0.75 m. Some scholars also used pixel migration tracking technology, optical image registration and other related technologies to study the earthquake. At the same time, based on the above research and combined with GNSS data, the slip distribution inversion was carried out. The results show that the earthquakes are mainly sinistral strike-slip. However, fault partitioning schemes are inconsistent and results vary widely. Finally, the coulomb stress of coshock is calculated and the possibility of future earthquakes in this area is studied [34,35,37–42].

The following research objectives were addressed in this study: First, the coseismic deformation field of the earthquake was obtained using Sentinel-1 SAR imagery. Then, a rectangular dislocation model based on an elastic half-space was used to estimate the coseismic slip distribution of the seismogenic fault in this earthquake. Finally, The Coulomb stress changes caused by the earthquake to the surrounding faults were calculated using the coseismic slip distribution. The seismic hazards of the primary faults in the study area were then analyzed.

2. Data processing and coseismic deformation field

2.1. Data sources

This study used freely released Sentinel-1 SAR satellite imagery from the European Space Agency. The satellite imagery offers an image coverage of up to 250 km, a spatial resolution of 5 m × 20 m, and a review period of at least 6 days. Sentinel-1 employs a strict orbit control technology to ensure a small space baseline, leading to a high coherence of the obtained interferogram. Hence, Sentinel-1 imagery is an effective data source for InSAR technology to monitor a wide range of surface deformation.

In this study, Sentinel-1 satellite data were used to obtain the coseismic deformation field of the 2022 Menyuan M_S6.9 earthquake. These data from 33 tracks for the descending orbit, and 128 and 26 tracks for the ascending orbit, respectively. The details of the data are shown in Table 2.

2.2. Data processing

InSAR data was processed using the D-InSAR two-orbit method on the Swiss GAMMA software platform. The external DEM used to eliminate the terrain phase was SRTM DEM with a 30 m resolution published by NASA. As the spatial baseline of the image pair is relatively small, the effect of DEM error on the deformation result should be considered.

The SAR data was registered using the enhanced spectral classification method, achieving a registration accuracy of one-thousandth pixel. The multiple look ratio used was 10:2. To improve the coherence of the interferogram, the Goldstein method was applied twice [43], using a filtering window size of 64 × 64 and 32 × 32, respectively. The minimum cost flow method based on the Delaunay triangle network was then used to phase untangle the interferogram. The stable point with high coherence, which was relatively far away from the deformation region, was selected as the reference point for unwrapping. The unwrapping threshold was set to 0.1, and the deformation phase map was then obtained. To estimate and remove the atmospheric delay error, a linear model related to the terrain was employed [44]. The deformation phase was then converted into displacement and geocoded to acquire the coseismic deformation field in the LOS direction of the satellite.

2.3. InSAR coseismic deformation field

Based on the coseismic deformation field obtained Fig. 2d, f, the T33 descending orbit image data provided complete coverage of the deformation area of the earthquake, resulting in a symmetric butterfly-shaped deformation field. The T128 ascending orbit image data thoroughly covered the coseismic deformation, whereas the T26 ascending orbit image data only partially covered the earthquake area. In general, the deformation field predominantly spreads on both sides of the western end of the Lenglongling fault and extends westward to the Tuolaishan fault. The interferogram demonstrates Fig. 2a–2c relatively high coherence of the entire deformation field, except the deformation center area, where the deformation gradient near the fault is too high, resulting in low coherence and incoherence in some areas. This indicates that the coseismic rupture of this earthquake has reached the surface. A comparison of the coseismic deformation fields obtained from the three orbits shows opposite deformation trends between the north and south plates of the coseismic deformation field of the lifting rail. The north and south walls of the deformation field in the same orbit also exhibit opposite motion states, indicating that the earthquake is predominantly characterized by strike-slip motion.

To further analyze the coseismic deformation characteristics of the earthquake, three section lines of 11′, 22′ and 33′ were respectively made through the maximum deformation area of the three deformation fields. The shape variables of these section lines Fig. 3a–3c and the white lines in Fig. 2d–2f were obtained. The maximum displacement of the deformation field in the LOS direction was 0.59 m, with a minimum displacement of −0.48 m. The maximum displacement in the LOS direction obtained by the T128 ascending rail image was 0.43 m, and the minimum displacement was −0.62 m. The maximum displacement in the LOS direction of the deformation field obtained by the T26 ascending rail image was 0.18 m, and the minimum displacement was −0.62 m. The difference in the minimum deformation between Track 26 and Track 128 was 0.01 m.

3. Inversion of fault slip distribution

The coseismic deformation field of the 2022 Menyuan earthquake was used as a constraint to calculate the coseismic slip distribution of the fault. The inversion algorithm used in this study was the SDM method proposed by Wang et al. [10]. The principle is based on the gradient descent method for inversion calculation. The main idea is to use the negative gradient direction to determine the new search direction of each iteration to ensure that the

Table 2
Key information on the Sentinel-1 imagery used in the study.

orbit number	classification of track	acquisition time		time-baseline (d)	Spatial baseline (m)
		Master image (Year-Month-Day)	Generated image (Year-Month-Day)		
		pre-earthquake	Post-earthquake		
T128	ascending	2022-01-05	2022-01-17	12	38
T26	ascending	2021-12-19	2022-01-10	12	−110
T33	descending	2021-12-19	2022-01-10	12	55

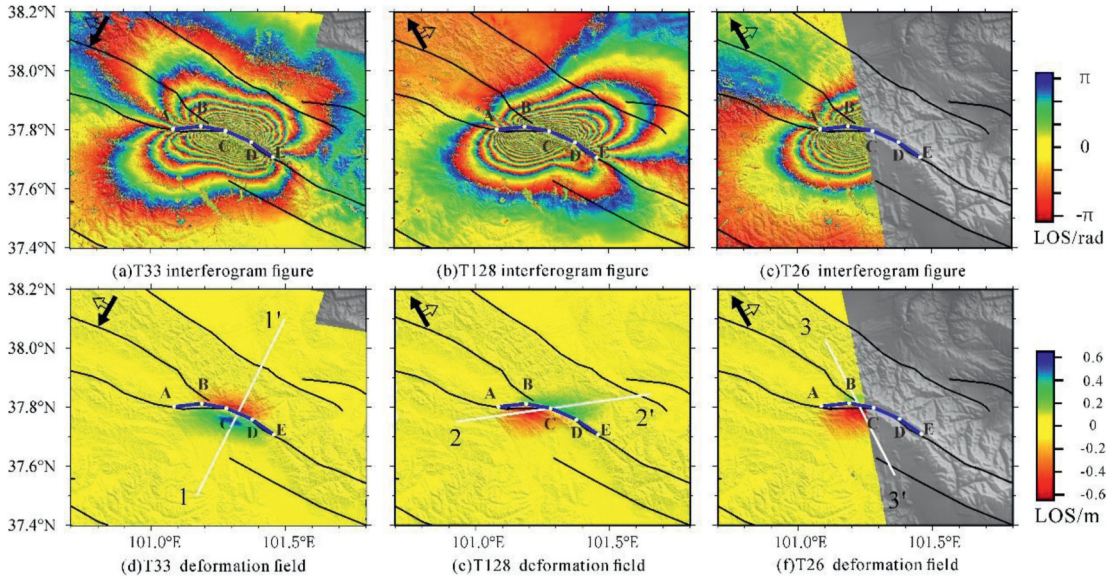

Fig. 2. InSAR coseismic deformation field of the 2022 Menyuan earthquake. The blue solid line indicates the location of the inversion fault, the solid white line is the section line position, the solid black line is the fault location, the black solid arrow indicates the direction of the satellite's flight, and the black hollow arrow indicates the direction of the satellite's line of sight.

objective function to be optimized is gradually reduced at each iteration.

The coseismic deformation field obtained by InSAR technology has a relatively high spatial resolution. If all data points had participated in the inversion, the calculation amount would have been relatively large and the inversion time would have been long, and the efficiency would have been low. The noise in the deformation field made it difficult to converge the inversion results. Therefore, this study used the uniform sampling method downsample the coseismic deformation field, which effectively reduced the amount of data and ensured smooth inversion. In the sampling process, the density of sampling points increased in the concentrated area for deformation, and the density of sampling points was reduced away from the deformation area.

In terms of setting the fault geometry, the InSAR coseismic deformation field can provide a basis for judging the seismogenic faults of earthquakes [45–54]. Therefore, based on the InSAR coseismic deformation boundary and the existing locations of the Lenglongling fault and the Tuolaishan fault, the inversion fault was divided into 4 segments (Fig. 2): AB, BC, CD, and DE, with the lengths corresponding to 9.2 km, 8.2 km, 9.4 km, and 9 km, respectively. The Tuolaishan fault and the Lenglongling fault belong to high angle strike-slip faults, and the dip angle of faults was set at 80°, referring to the published research results of Li et al. (2022) [55]. As this paper only focused on the shallow slip state of the fault, the depth of the model was set as 20 km. The resolution of the fault along the dip was set at 2 km, and the resolution along the strike was set at 1 km, which was divided into a rectangular grid of 2 km × 1 km. In the coseismic slip distribution inversion, given that the data from the three deformation fields used in the coseismic slip inversion were all InSAR data with the same quality, the weight of the lifting and descending orbit data was set to 1:1:1. In addition, it is also necessary to search for the smoothing factor to determine the optimal calculation model. The smoothing factor was determined by searching the posterior variance of the model under different smoothing factors. The results in Fig. 4 show that a larger smoothing factor corresponds to a larger residual model fitting error. As the smoothness factor decreased, the smoothness increased, and the fitting residual decreased. However, when the smoothing factor was too small, the improvement of the fitting results was very limited and may affect the objective authenticity of the inversion results. Consequently, we have determined a smoothing factor of 0.15.

The fault slip distribution obtained via inversion is shown in Fig. 5. The diagram shows that the main slip distribution of the fault

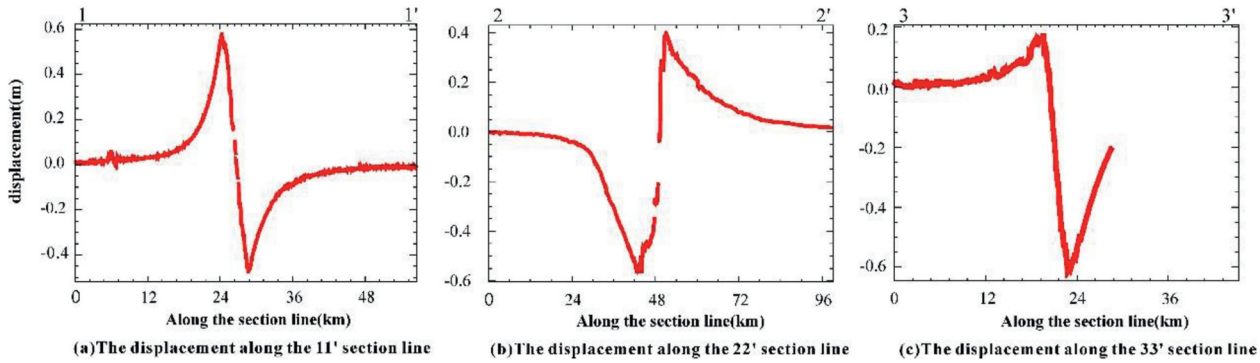

Fig. 3. Deformation along the section line.

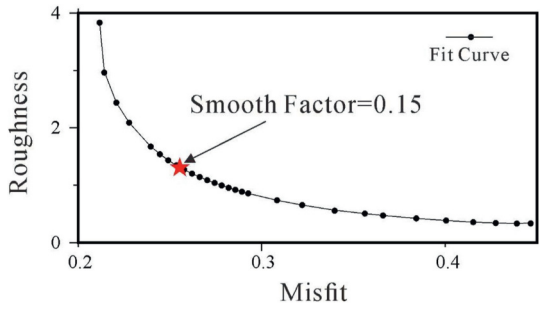

Fig. 4. Curve of the smoothing factor selected in the inversion model. The black dots represent different smoothing factor values. The red pentagram represents the preferred smoothing factor for the inversion model.

occurred in the BC and CD segments. Two fault slip distributions were observed in the AB segment along the dip (2–6 km) and strike (1–8 km), and along the inclination (12–20 km) and strike (1–8 km). The maximum slippage occurred 2 km and 12–16 km below the surface, respectively, with the maximum slippage reaching 1.25 m. The maximum slippage in the BC segment was distributed 6 km along the trend and 5 km along the strike, with the maximum slippage measuring 4.09 m. The maximum slippage distribution of the CD segment was concentrated at 4–6 km along the dip and 3–6 km along the strike, with the maximum slippage measuring 4.51 m. The slippage of the DE segment was relatively small and was predominantly distributed at 2–7 km along the strike of dip 4–12 km, with a maximum slippage of 0.79 m. In the BC and CD segments, the fault slip distribution reached the surface, implying that the total length of the surface rupture was approximately 16 km. The moment magnitude of the earthquake was calculated to be M_W6.7.

Fig. 6 shows the observed values, simulated values, and residual distribution of Track T128, Track T26, and Track T33, respectively. The simulation results fit the observation results with a degree of fit of 97%. The residual values of the fitting were primarily distributed in the range of 0–200 mm and are primarily concentrated in in the center of the deformation field. This was because the deformation gradient in the center of the deformation field is too large, and low coherence leads to unwrapping errors.

To verify the reliability of the inversion results, a checkerboard was established as the input model. This was undertaken to test the resolution of the inversion based on the faults used in slip distribution inversion (Fig. 7). Fig. 7a shows the input slip model, where the red square represents a test cell measuring 4 km along the fault strike and 4 km along the dip, with a slip of 1 m. Blue squares indicate test cells 4 km along the fault strike and 4 km along the dip, with no slip (0 m). Using forward modeling, this paper obtained the surface deformation field, and then used SDM under the constraint of the deformation field to invert the checkerboard slip distribution. The inversion parameters remained consistent with fault slip distribution inversion; the results are shown in Fig. 7b. The inversion results indicate good conformity with the input checkerboard model at approximately 0–12 km along the fault dip, indicating a better fitting effect of the slip distribution of the fault plane in this section. However, at approximately 12–20 km along the fault dip, the resolution is low, and the fitting effect of the slip distribution of the fault plane is relatively poor.

4. Coulombic stress

After the earthquake, the public was concerned whether the current earthquake had caused the rupture and whether further earthquakes would occur. To address these concerns, calculated the Coulomb stress changes generated by the Menyuan earthquake in 2016 and the Menyuan earthquake in 2022 using the coseismic sliding model. The PSGRN/PSCMP program presented by Wang et al. [56] and the layered viscoelastic medium model was used to calculate Coulomb stress changes. In this study, considered the Lenglongling fault and its 23 surrounding faults as receiving faults, set the parameters of the receiving fault regarding the relevant historical seismic data, and new tectonic data from the area, and the data on static Coulomb stress change [57,58] (Table 3). In this paper set the friction coefficient of the receiving fault as 0.3 and obtained the influence of the Menyuan earthquakes in 2016 and 2022 on the surrounding active faults.

Fig. 8b shows the influence of the 2022 Menyuan M_S6.9 earthquake on the main active faults in the study area, which indicates that the earthquake had a considerable loading effect of up to 0.1 Mpa on the Tuolaishan fault and the Lenglongling fault. Moreover, the earthquake also had a substantial loading effect on the Minle–Damaying fault to the north of the epicenter, the western section of the Dabanshan fault to the south, and the northern section of the Riyueshan fault to the west. Furthermore, the earthquake had a certain loading effect on the Jinqianghe–Haiyuan fault, Menyuan fault, Sunan fault, Gulang fault, the southern and northern margin faults of Laji Mountain, the Yumushan fault, and the Longshoushan fault. It also had a certain unloading effect on the western section of the Huangcheng–Shuangta fault, the western section of the Minle Yongchang fault, the eastern section of the Dabanshan fault, and the Muli–Jiangcang fault.

In addition to these issues, there is also a seismogenic fault along the Lenglongling fault, where a M_W5.9 earthquake occurred in 2016. The 2016 earthquake and the earthquake has triggered the relationship, which is another considerable concern. To investigate this, we used the InSAR deformation field of the 2016 Menyuan earthquake to retrieve the fault slip model and calculate the coseismic and post-seismic Coulombic stresses, assuming a viscosity of 8×10^{18} Mpa [59,60]. The calculation results are shown in Fig. 8a, which shows that the 2016 Menyuan earthquake had a

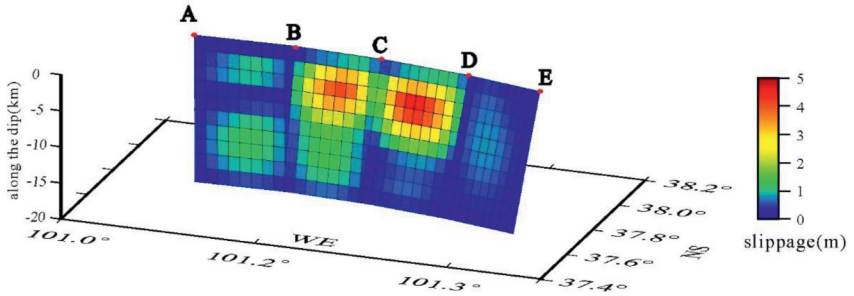

Fig. 5. Coseismic slip distribution of seismogenic faults in the 2022 Menyuan earthquake.

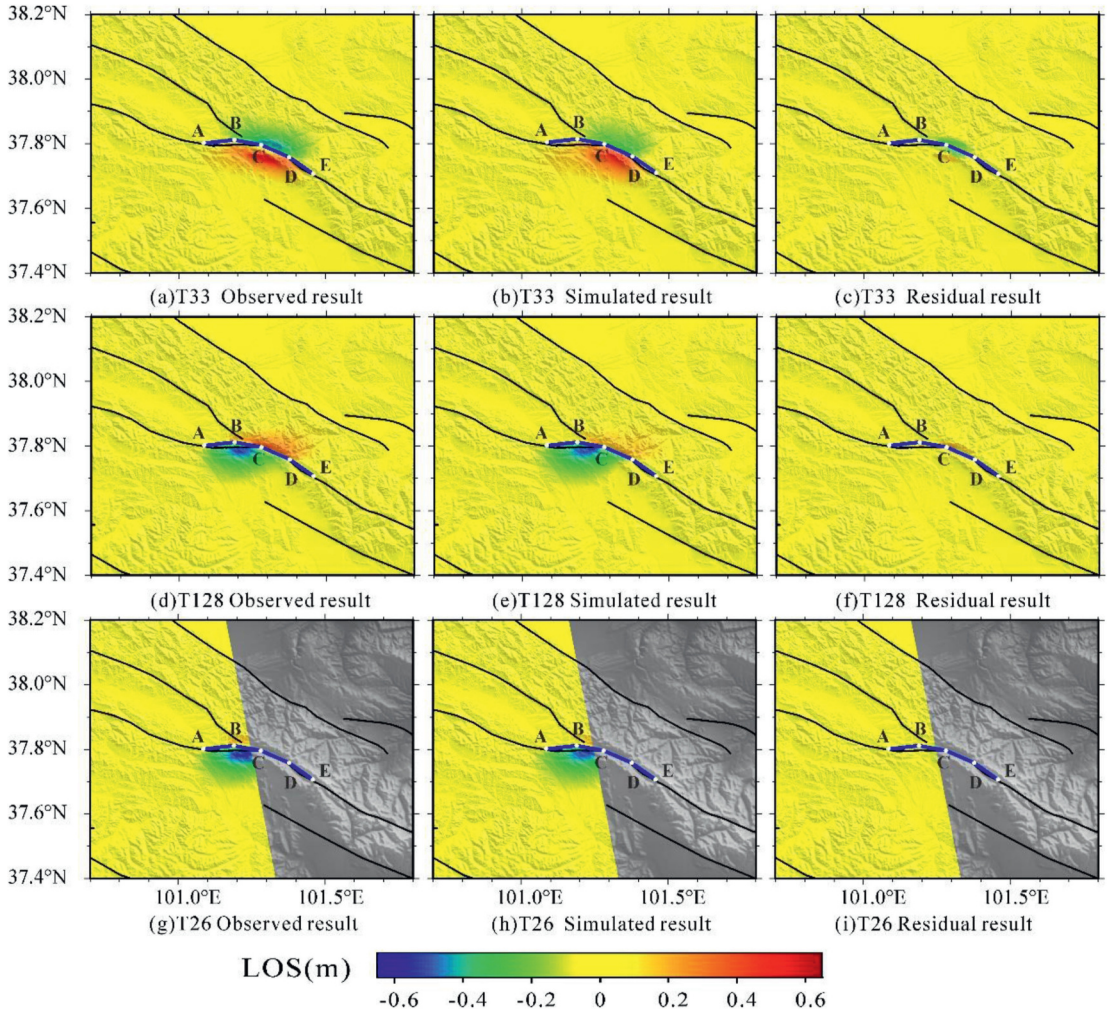

Fig. 6. Deformation field and residual error of optimal sliding model fitting. The blue solid line is the fault surface projection track. The solid black lines are tectonic fractures in this area.

strong loading effect on the Tuolaishan fault, Lenglongling fault, and the Jinqianghe–Haiyuan fault.

5. Discussion

The InSAR coseismic deformation field is a fundamental tool for identifying the seismogenic faults associated with earthquakes. By comparing the three coseismic deformation fields (Fig. 2), it is found that the deformation is distributed along the western end of the Lenglongling fault and the eastern end of the Tuolaishan fault. The southern and northern disks move in opposite directions. In the ascending orbit deformation field, the southern fault wall moves away from the satellite LOS, whereas the northern fault wall moves closer to the LOS. In the descending orbit deformation field, the southern fault wall moves closer to the satellite LOS, and the northern fault wall moves away from the satellite LOS. Both sides of the fault in the deformation field of the same orbit showed opposite motion states. This phenomenon indicates that the earthquake was dominated by left-lateral horizontal motion.

Furthermore, the maximum value of the deformation field is consistent with the precision location result of the main earthquake, and both are located in the west section of Lenglongling.

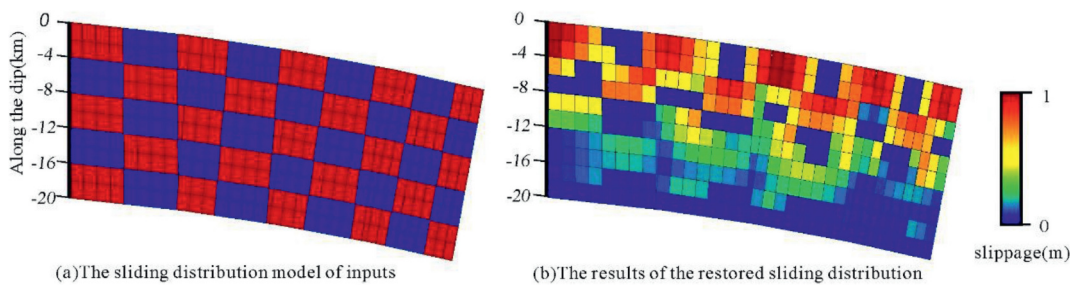

Fig. 7. Data resolution test board.

Table 3
Information on the Lenglongling fault and its surrounding faults.

Fault name	strike (°)	dip angle (°)	angle of slip (°)	Effective friction coefficient
Tuolaishan fault	110	80	0	0.3
Lenglongling fault	115	80	0	0.3
Jinqianghe fault	110	80	0	0.3
The southern margin fault of Maomaoshan	110	80	0	0.3
Maomaoshan-Laohushan fault	110	80	0	0.3
Xiangshan-Tianjing fault	104	60	7	0.3
Huangcheng–Shuangta fault	285	45	90	0.3
Minle–Damaying fault	298	30	90	0.3
Sunan – Qilian fault	300	60	90	0.3
Minle Yongchang fault	311	14	82	0.3
North fault of Yumushan	335	60	133	0.3
East fault of Yumushan	290	60	114	0.3
Eastern section of the south margin of Longshou shan	307	55	110	0.3
Western section of the south margin of Longshou shan	298	55	110	0.3
Dabanshan fault	310	80	0	0.3
Menyuan fault	300	60	90	0.3
Mayaxueshan fault	135	60	90	0.3
Zhiwuanglanghe fault	110	55	90	0.3
Riyueshan fault	160	80	176	0.3
Muli–Jiangcang fault	120	80	0	0.3
The southern margin fault of Laji Mountain	120	50	60	0.3
The northern margin fault of Laji Mountain	120	50	80	0.3

This not only validates the reliability of the InSAR results but also indicates that the seismogenic fault responsible for this earthquake is the left-lateral strike-slip Lenglongling fault. After the main earthquake occurred in the western section of the Lenglongling fault, it extended eastward along the Lenglongling fault and ruptured along the eastern segment of the Tuolaishan fault toward the west.

The aftershock precision location results [61] within 9 days after the 2022 Menyuan earthquake are distributed in the InSAR deformation field Fig. 9a. The distribution of aftershocks can be divided into two parts. One part coincides with the fault trace in the Lenglongling fault, and the other substantially deviate from the fault trace represented by deformation. The AA' profile has a depth of 20 km and a length of 20 km (blue line in Fig. 9a). The AA' profile (Fig. 9b) shows that the main aftershock is located on the AA' profile. However, there is a substantial deviation between the main aftershock and the fault trace of the InSAR deformation field in the AA' section, which indicates that the dip angle of the seismogenic fault is not 90°. Section line BB' was obtained by taking a point on the surface of the AA' profile and extending 10 km to the north and south with a depth of 20 km, as shown in Fig. 9c.

In Fig. 9 c, the position of the blue line is the intersection of BB' and AA', and the position of the red line is the intersection of BB' and the fault trace of the deformation field. The aftershocks are vertically distributed and coincide with the blue line. There are two reasons for this phenomenon. One is related to the accuracy of the aftershock location, and the other is related to the tectonic background of the epicenter. From the perspective of the geological structure, the Tuolaishan fault and Lenglongling fault are two left-lateral strike-slip faults, forming a left-lateral left order microtension type order area. In the order area, a hidden fault is parallel to the Lenglongling fault. After the earthquake, the hidden fault activity in the order area produced many aftershocks. It is not uncommon for faults to develop in such a zone. Ye et al. (2017) used numerical simulation techniques to confirm that the concealed faults developed in the Greater Bay Area of Southern California absorbed a substantial amount of strike-slip motion [60]. Liu et al. (2021) summarized the decomposition effect of the tail end of the

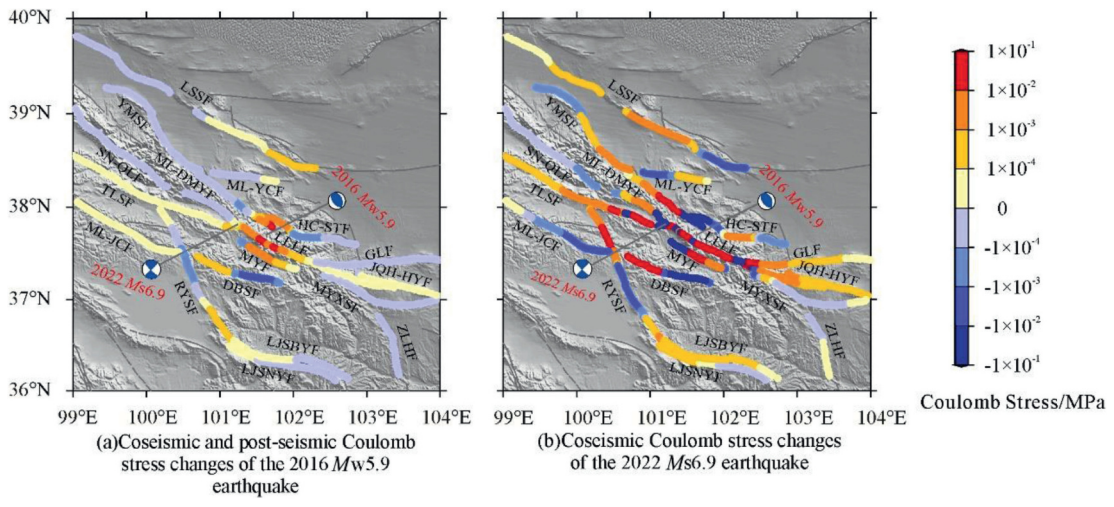

Fig. 8. Coulomb stress changes caused by the 2016 Menyuan earthquake and the 2022 Menyuan earthquake.

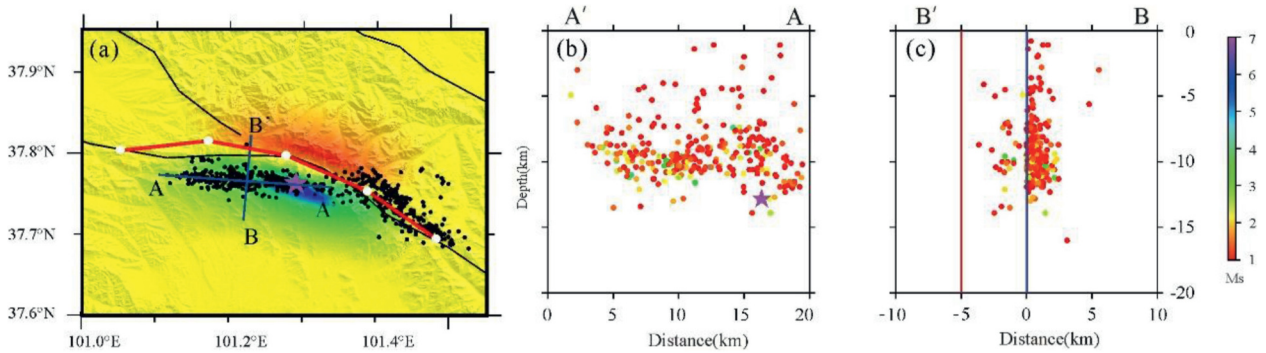

Fig. 9. Aftershock distribution from the 2022 Menyuan earthquake. (a) Coseismic deformation field and aftershock distribution of orbit 33; the red broken line represents the fault trace of InSAR coseismic inversion results, the white dots represent turning points of inversion faults, and the black dots represent aftershock distribution after precise location. (b) Aftershock distribution along A'A profile line, the purple five-pointed star represents the epicenter of the main earthquake. (c) Aftershock distribution along B'B profile line, the red line represents the position of the deformation track in the coseismic deformation field, and the blue represents the concentrated location of the aftershocks.

strike-slip fault on the slip rate, in which branch faults developed in the left-lateral left order release zone are also a relatively common occurrence [62].

Many scholars have used InSAR technology and sentinel-1 satellite image to study the earthquake. Xu et al. (2022) used InSAR technology to calculate the co-seismic deformation field of three orbits, namely, orbit ascension T26, orbit 128, and orbit descent T33, of the sentinel-1 satellite, and the magnitude of the deformation reached approximately 0.60 m. The co-seismic displacement (LOS) of ascending and descending rails shows opposite deformation characteristics. At least two faults have ruptured, with the main fault corresponding to the western section of the Lenglongling fault. Yang et al. [38] and Li et al. [55] analyzed the co-seismic deformation field of the earthquake using post-earthquake T33 orbit images. The results show that the main surface rupture occurred on the Lenglongling fault; the surface rupture length is approximately 22 km, and the horizontal dislocation is approximately 0.50 m. Feng et al. [33] and Lu et al. [34] used InSAR and pixel offset tracking. They obtained co-seismic displacements along line-of-sight and near-field range offsets of this earthquake. The maximum line-of-sight deformation is 0.61 m, and the maximum distance deviation of surface rupture is 0.79 m. Yu et al. [34] used InSAR technology to calculate the co-seismic deformation field of this earthquake, and the maximum deformation was approximately 0.75 m. They also obtain the east-west co-seismic deformation field of this earthquake using Sentinel-2 satellite data, optical image registration, and related technologies, and obtained a maximum co-seismic displacement of 2.5 m.

The co-seismic slip distribution shows that the seismogenic fault of the 2022 Menyuan earthquake is a high-dip strike-slip fault dominated by left-lateral strike-slip. The coseismic slip of this earthquake was predominantly concentrated in the western section of the Lenglongling fault. The epicenter area was relatively shallow and less than 20 km in depth, showing the characteristics of shallow east and deep west sections. The part of the coseismic slip greater than 1.5 m is within 12 km depth. The maximum displacement of the optimal coseismic model is 4.51 m, and the maximum slip is located at a depth of 5 km. The moment magnitude obtained by inversion is M_W6.7.

Many scholars used the co-seismic deformation field obtained using InSAR technology as the constraint to invert the slip distribution of seismogenesis faults; however, the partition scheme of seismogenesis faults is different. The inversion fault model used in this study is similar to that used by Li et al. [55] and Lu et al. [34], which divides the fault into two parts, one located in the western section of the Lenglongling fault and the other extending to the Tuolaishan fault. Nonetheless, the inversion fault located in the Lenglongling fault is divided into three parts in this study, which is a more refined scale. Li et al. used Sentinel-1 descending orbit T33 and ascending orbit T26 data, whereas Lv et al. used descending orbit T33 and ascending orbit T128 combined with high-frequency GNSS data [34,55]. This study used Sentinel-1 descending rail T33, ascending rail T26, and ascending rail T26 data. Although ascending rail T26 images only provide a partial seismic surface deformation field, the ascending rail SAR image is complementary to the surface deformation imaging of strike-slip fault rupture. Therefore, it has a stronger slip-restraint ability. In terms of inversion results, there are two deformation centers in the results of Li et al. [55] and Lv et al. [34], which are located at the Lenglongling fault and the Tuolaishan fault, respectively. The inversion by Lv et al. [34] shows that the maximum slip is located at the Lenglongling fault, with a maximum slip of approximately 4 m and a depth of approximately 4 km. There is a small high-slip zone in the Tuolaishan fault, with a maximum slip of approximately 2 m and a corresponding depth of 4 km. The results of Li et al. [55] show that the slip is primarily concentrated in an underground area of 2–7 km, and the maximum slip of the fault is 3.5 m and occurs approximately 4 km underground. There are also areas of slip at the Tuolaishan fault.

Other observations have also been used to study the earthquake. Li et al. [8] obtained the fault rupture slip distribution model by inversion based on the co-seismic deformation field obtained by the discrete GNSS station. In terms of fault model setting, Li et al. [8] established three fault models, namely, Tuolaishan, Changma-Erbo, and Lenglongling models. However, in this study, only two fault models were established, namely, the models for the western section of the Lenglongling fault and the eastern section of the Tuolaishan fault. The length of the fault model is shorter than that of Li et al. [8]. The results show that the fault slip is primarily distributed in the western section of the Lenglongling fault and the eastern section of the Tuolaishan fault. The significant fault rupture slip is primarily concentrated at a depth of 8 km below the surface; the maximum slip is approximately 3 m, and the focal point of the main earthquake is located at the lower edge of the maximum slip.

The results of this study show that the maximum slip is 4.51 m, and the slip distribution is primarily concentrated in the range of 2–10 km, which is slightly different from the results of the above scholars. However, the locations of the maximum slip are consistent with the locations of the main earthquake, and the fault slip is concentrated in the western section of the Lenglongling fault and the eastern section of the Tuolaishan fault, which has a good spatial consistency with the seismic precision location results.

In this study, there are two sliding regions in the Lenglongling fault, and the range of the two sliding regions along the strike is essentially consistent with the results of the above scholars. In the Tuolaishan fault, compared with the results reported by the above scholars, there is an additional smaller sliding region at a depth of 12–20 km underground. Via checkerboard test, it is proved that the fitting degree of this area is not good, which can be considered as an error.

From the coseismic static Coulomb stress of the earthquake, it is found that the earthquake had a considerable loading effect on the Tuolaishan fault to the west of the epicenter and the Lenglongling fault to the east of up to 0.1 Mpa (Fig. 8b). Therefore, the Tuolaishan fault is likely the subsequent fault with a high probability of earthquakes occurring after this earthquake. The earthquake also had a substantial loading effect on the Minle–Damaying fault due north of the epicenter, the western section of the Dabanshan fault due south, and the northern section of the Riyueshan fault to the west, and the risk is worthy of attention. An M_W5.9 magnitude earthquake occurred in 2016 on the secondary fault on the northern side of the Lenglongling fault, approximately 40 km from the epicenter of this earthquake. By calculating the coseismic and post-seismic Coulombe stress of the 2016 Menyuan earthquake (Fig. 8a), it has been found that the 2016 Menyuan earthquake has a strong loading effect on the Tuolaishan fault, Lenglongling fault, and the Jinqianghe–Haiyuan fault. It is calculated that coseismic dislocation and post-earthquake viscous relaxation effect of the 2016 Menyuan earthquake increase the cumulative Coulomb stress at the epicenter of the 2022 Menyuan earthquake by 1013 Pa, which promoted the occurrence of the 2022 Menyuan earthquake, with the coseismic effect playing a substantial role, whereas the post-earthquake viscous relaxation effect exerted a relatively minor effect.

6. Conclusions

(1) Combining the InSAR deformation boundary and the aftershock profile, it is likely that the seismogenic fault of this earthquake is the west end of the Lenglongling fault. The length of the coseismic deformation field is approximately 25 km in the north–south direction and 35 km in the east–west direction. When the satellite LOS was upward, the maximum deformation quantity of the south wall and the north wall was 0.62 m and 0.48 m, respectively. The type of earthquake was left-lateral strike-slip.

(2) The inversion results from the coseismic slip distribution show that the seismogenic fault from the 2022 Menyuan earthquake is a left-lateral strike-slip fault with a high dip angle. The maximum slip magnitude can reach up to 4.51 m, and the maximum slip is located at 5 km along the inclination.

(3) The calculation results from the coseismic static Coulomb stress of the 2022 Menyuan earthquake show that the Menyuan earthquake had a substantial loading effect of up to 0.1 Mpa on the Tuolaishan fault to the west of the epicenter and the Lenglongling fault to the east. The results show that the Tuolaishan fault is the subsequent fault with a high probability of the next earthquake after the earthquake being examined.

(4) The coseismic and post-seismic Coulomb stress calculations from the 2016 Menyuan earthquake show that the 2016 Menyuan earthquake promoted the 2022 Menyuan earthquake, in which the coseismic effect played a substantial role, and the post-earthquake viscous relaxation effect had a relatively minor effect.

Author statement

All persons who have made substantial contributions to the work reported in the manuscript, and reviewed and approved the manuscript. All funds supporting this research were acknowledged in the acknowledgements section, and all data involved in this study were also acknowledged.

Conflicts of interest

The authors declare that there is no conflicts of interest.

Acknowledgements

This research was supported by the Natural Science Foundation of China (Grant Nos. 42104061) Shaanxi Province natural science basic research program (Grant Nos. 2023-JC-QN-0296) and Science for Earthquake Resilience (Grant Nos. XH23059YA). The European Space Agency provided Sentinel-1 radar data for this study, Prof. Wang Rongjiang from the German Research Center for Earth Sciences provided the SDM inversion program, and Dr. Fang Lihua from the Institute of Geophysics, China Earthquake Administration provided the aftershock precision location results. I would like to express my gratitude to them.

References

[1] H.B. Li, J.W.J.W. Pan, Z.M. Sun, et al., Continental tectonic deformation and seismic activity: a case study from the Tibetan plateau, Acta Geol. Sin. 95 (1) (2021) 194–213.
[2] Y.C. Li, J. Nocquet, X. Shan, et al., Geodetic observations of shallow creep on the laohushan Haiyuan fault, northeastern tibet[J], J. Geophys. Res. Solid Earth 126 (6) (2021).
[3] W.J. Zheng, B.X. Zhang, D.Y. Yuan, et al., Tectonic activity in the southern alashan block and the latest boundary of outward expansion on the northeastern Tibetan plateau, China[J], J. Earth Sci. Environ. 43 (2) (2021) 224–236 [in Chinese].
[4] D.Y. Yuan, W.P. Ge, Z.W. Chen, C.Y. Li, Z.C. Wang, H.P. Zhang, et al., The growth of northeastern tibet and its relevance to large scale continental geodynamics: a review of recent studies, Tectonics 32 (2013) 1358 1370.
[5] W.G. He, D.Y. Yuan, W.P. Ge, et al., Determination of the slip rate of the Lenglongling Fault in the middle and eastern segments of the qilian mountain active fault zone[J], Earthquake 30 (1) (2010) 131–137.
[6] C. Lasserre, Y. Gaudemer, P. Tapponnier, et al., Fast late pleistocene slip rate on the LengLongLing segment of the Haiyuan fault, Qinghai, China, J. Geophys. Res. 107 (B11) (2002) 2276, https://doi.org/10.1029/2000JB000060.
[7] P. Guo, Earthquake recurrence behavior and seismic hazards of the Lenglongling Fault, northern qilian Shan [D], Institute of Geology, China Earthquake Administration, 2019 [in Chinese].
[8] Y.H. Li, M. Liu, et al., Present-day crustal deformation and strain transfer in northeastern Tibetan Plateau[J], Earth Planet Sci. Lett.: A Letter Journal Devoted to the Development in Time of the Earth and Planetary System 487 (2018) 179–189.
[9] O. Cavalie, C. Lasserre, M.P. Doin, et al., Mea-surement of interseismic strain across the Haiyuan fault (gansu, China), by InSAR, Earth Planet Sci. Lett. 275 (3–4) (2008) 246–257.
[10] R.J. Wang, F.Q. Diao, A. Hoechner, SDM - a geodetic inversion code incorporating with layered crust structure and curved fault geometry[J], EGU General Assembly Conference Abstracts, 2013.
[11] S. Daout, R. Jolivet, C. Lasserre, et al., Along-strike variations of the partitioning of conver-gence across the Haiyuan fault system detected by InSAR, Geophys J. Int 205 (1) (2016) 536–547.
[12] C.Z. Hu, X.P. Yang, Z.M. Li, et al., Seismogenic mechanism of the 21 January 2016 Menyuan, Qinghai MS6.4 earthquake[J], Chin. J. Geophys. 59 (5) (2016) 1637–1646 [in Chinese].
[13] P. Guo, Z.J. Han, Y.F. An, et al., Activity of Lenglongling Fault system and of the 2016 earthquake[J], Sci. China Earth Sci. 47 (5) (2017) 617–630.
[14] W. Xiong, W. Chen, B. Zhao, et al., Insight into the 2016 Menyuan Mw 5.9 earthquake with InSAR: a blind reverse event promoted by historical earthquakes[J], Pure Appl. Geophys. 176 (2) (2019) 577–591.
[15] Y. Liu, C.J. Xu, Y.M. Wen, InSAR observation of Menyuan Mw5.9 earthquake deformation and deep geometry of regional fault zone[J], Geomatics Inf. Sci. Wuhan Univ. 44 (7) (2019) 1035–1042 [in Chinese].
[16] Y. Liu, G. Zhang, Y. Zhang, et al., Source parameters of the 2016 Menyuan earthquake in the northeastern Tibetan plateau determined from regional

seismic waveforms and InSAR measurements[J], J. Asian Earth Sci. 158 (2018) 103–111.
[17] Y.F. Zhang, X. Shan, G. Zhang, et al., The 2016 Mw 5.9 Menyuan earthquake in the qilian orogen, China: a potentially delayed depth egmented rupture following from the 1986 Mw 6.0 Menyuan earthquake[J], Seismol Res. Lett. 91 (2A) (2020) 758–769.
[18] W. Qu, B. Liu, Q. Zhang, et al., Sentinel-1 InSAR observations of Co- and post-seismic deformation mechanisms of the 2016 Mw 5.9 Menyuan Earthquake,Northwestern China[J], Adv. Space Res. 68 (3) (2021) 1301–1317, https://doi.org/10.1016/j.asr.2021.03.016.
[19] S.S. Liang, J.S. Lei, Z.G. Xu, L.Y. Zuo, J.G. Liu, Relocation of the aftershock sequence and focal mechanism solutions of the 21 January 2016 Menyuan, Qinghai, MS6.4 earthquake, Chin. J. Geophys. 60 (6) (2017) 2091–2103, https://doi.org/10.6038/cjg20170606 [in Chinese].
[20] Y.F. Zhang, X.J. Shan, G.H. Zhang, et al., The 2016 Mw 5.9 Menyuan earthquake in the Qilian Orogen, China: a potentially delayed depth-segmented rupture following from the 1986 Mw 6.0 Menyuan earthquake, Seismol Res. Lett. 91 (2020) 758–769.
[21] Z.H. Li, B.Q. Han, Z.J. Liu, et al., Source parameters and slip distributions of the 2016 and 2022 Menyuan, Qinghai earthquakes constrained by InSAR observations, Geomatics Inf. Sci. Wuhan Univ. 47 (2022) 887–897 [in Chinese].
[22] C.Z. Hu, P.X. Yang, Z.M. Li, et al., Seismogenic mechanism of the 21 January 2016 Menyuan, Qinghai Ms6.4 earthquake, Chin J Geophys 59 (2016) 1637–1646 [in Chinese].
[23] M. Liu, H.Y. Li, Z.G. Peng, et al., Spatial-temporal distribution of early aftershocks following the 2016 Ms6.4 Menyuan, Qinghai, China earthquake, Tectonophysics 766 (2019) 469–479.
[24] Y.H. Liu, G.H. Zhang, Y.F. Zhang, et al., Source parameters of the 2016 Menyuan earthquake in the northeastern Tibetan Plateau determined from regional seismic waveforms and InSAR measurements, J Asian Earth Sci 158 (2018) 103–111.
[25] D. Massonnet, M. Rossi, C. Carmona, et al., The displacement field of the landers earthquake Mapped by radar interferometry[J], Nature 364 (6433) (1990) 138–142.
[26] X.J. Shan, C.Y. Qu, W.Y. Gong, et al., Coseismic deformation field of the Jiuzhaigou MS7.0 earthquake from Sentinel-1A InSAR data and fault slip inversion [J], Chin. J. Geophys. 60 (12) (2017) 4527–4536 [in Chinese].
[27] W.T. Zhang, L.Y. Ji, L.Y. Zhu, et al., A typical thrust rupture event occurring in the foreland basin of the southern Tianshan:The 2020 Xinjiang Jiashi Ms6.4 earthquake [J], Seismol. Geol. 43 (2) (2021) 394–409 [in Chinese].
[28] J.R. Elliott, R.J. Walters, P.C. England, et al., Extension on the Tibetan plateau: recent normal faulting measured by InSAR and body wave seismology, Geophys. J. Int. 183 (2) (2021) 503–535.
[29] Z.H. Li, J.R. Elliott, W. Feng, et al., The 2010 Mw6.8 yushu (Qinghai, China) earthquake: constraints provided by InSAR and body wave seismology[J], J. Geophys. Res. 116 (B10) (2011), https://doi.org/10.1029/2011JB008358.
[30] J. Sun, Z.K. Shen, T. Li, et al., Thrust faulting and 3D ground deformation of the 3 july 2015 Mw 6.4 pishan, China earthquake from sentinel-1A radar interferometry[J], Tectonophysics. 683 (2016) 77–85, https://doi.org/10.1016/j.tecto.2016.05.051.
[31] C.J. Xu, P. He, Y.M. Wen, et al., Recent advances in SAR interferometry and its applications[J], Journal of Geomatics 40 176 (2) (2015) 1–9 [in Chinese].
[32] L.Y. Ji, C.J. Liu, J. Xu, et al., InSAR observation and inversion of the seismogenic fault for the 2017 Jiuzhaigou Ms7.0 earthquake in China[J], Chin. J. Geophys. 60 (10) (2017) 4069–4082 [in Chinese].
[33] W.P. Feng, S. Samsonov, Q. Qiu, et al., Orthogonal Fault rupture and rapid postseismic deformation following 2019 ridgecrest,California,earthquake sequence revealed from geodetic observations[J], Geophys. Res. Lett. 47 (5) (2020) e2019GL086888.
[34] M.Z. Lv, K.J. Chen, H.S. Chai, et al., Joint inversion of InSAR and high-rate GNSS displacement waveforms for the rupture process of the 2022 Qinghai Menyuan M6.9 earthquake, Chin. J. Geophys. 65 (12) (2022) 4725–4738 [in Chinese].
[35] P.F. Yu, W. Chen, X.J. Qiao, et al., Slip model of the 2022 Menyuan Ms6.9 earthquake constrained by Mulit-source SAR data[J], Geomatics Inf. Sci. Wuhan Univ. 47 (6) (2022) 898–906, https://doi.org/10.13203/j.whugis20220093 [in Chinese].
[36] R. Jolivet, C. Lasserre, M.P. Doin, et al., Shallow creep on the Haiyuan fault (gansu, China) revealed by SAR interferometry, J Geophys Res 117 (2012) B06401, https://doi.org/10.1029/2011JB008732.
[37] G.Y. Xu, X.W. Xu, Y.N. Yi, Y.M. Wen, Q.X. Wang, K. Li, et al., Seismogenic structure of the 2022 Menyuan MW6.6 earthquake, Qinghai Province, constrained by InSAR and gaofen-7 observation, Chin. J. Geophys. 65 (12) (2022) 4704–4724 [in Chinese].
[38] H.F. Yang, D. Wang, R.M. Guo, M.Y. Xie, Y. Zang, Y. Wang, et al., Rapid report of the 8 January 2022 MS6.9 Menyuan earthquake, Qinghai, China[J], Earthquake Research Advance 2 (1) (2022) 4–14, https://doi.org/10.1016/j.eqrea.2022.100113.
[39] W.P. Feng, X.H. He, Y.P. Zhang, L.H. Fang, S. Samsonov, P.Z. Zhang, Seismic faults of the 2022 Mw6.6 Menyuan, Qinghai earthquake and their implication for the regional seismogenic structures, Chin. Sci. Bull. 68 (2–3) (2023) 254–270, https://doi.org/10.1360/TB-2022-0154 [in Chinese].
[40] H. Luo, T. Wang, Strain partitioning on the western Haiyuan fault system revealed by the adjacent 2016 Mw5.9 and 2022 Mw6.7 Menyuan earthquakes, Geophys. Res. Lett. 49 (2022) e2022GL099348, https://doi.org/10.1029/2022GL099348.
[41] P. He, C.L. Liu, Y.M. Wen, X.P. He, K.H. Ding, C.J. Xu, The 2022 Mw6.6 Menyuan earthquake in the northwest margin of tibet: geodetic and seismic evidence of the fault structure and slip behavior of the qilian–haiyuan strike-slip fault, Seismol Res. Lett. (2022), https://doi.org/10.1785/0220220192.
[42] Y.S. Li, W.L. Jiang, Y.J. Li, W.H. Shen, Z.T. He, B.Q. Li, Q. Li, Q.S. Jiao, Y.F. Tian, Coseismic rupture model and tectonic implications of the January 7 2022, Menyuan Mw 6.6 earthquake constraints from InSAR observations and field investigation, Rem. Sens. (2022) 14, https://doi.org/10.3390/rs14092111.
[43] R.M. Goldstein, C.L. Werner, Radar interferogram filtering for geophysical applications[J], Geophys. Res. Lett. 25 (21) (1998) 4035–4038.
[44] C.S. Yang, Study on atmosphere delay correction methods in differential interferometric synthetic aperture radar[D], Chang'an University, 2011 [in Chinese].
[45] P.F. Yu, W. Xiong, W. Chen, et al., Slip model of the 2021 MS7.4 Madoi earthquake constrained by GNSS and InSAR coseismic deformation[J], Chin. J. Geophys. 65 (2) (2022) 509–522 [in Chinese].
[46] C. Saylor, J.B. Rundle, A. Donnellan, Multifractal analysis of a seismic moment distribution obtained from InSAR inversion[J], Earth Space Sci. 8 (9) (2021).
[47] X.B. Xu, C. Ma, S.Y. Hong, D.J. Lian, Y.F. Zhang, et al., Analysis of coseismic displacements due to the Mw7.8 Nepal earthquake using InSAR data and inversion of fault slip distribution[J], Earthquake 40 (4) (2020) 76–89 [in Chinese].
[48] W.P. Feng, L.S. Xu, Z.H. Xu, et al., Source parameters of the 2008 garze Mw6.4 and Mw5.9 earthquakes from InSAR measurements[J], Chin. J. Geophys. 52 (4) (2009) 983–993 [in Chinese].
[49] J.T. Qiu, L.Y. Ji, L. Liu, et al., InSAR coseimic deformation and tectonic implications for the 2020 Mw6.3 nima earthquake in xizang[J], Seismology and Egology 43 (6) (2021) 1586–1599 [in Chinese].
[50] C.Y. Qu, R.H. Zuo, X.J. Shan, et al., Coseismic deformation field of the Nepal Ms8.1 earthquake from Sentinel-1A/InSAR data and fault slip inversion[J], Chin. J. Geophys. 60 (1) (2017) 151–162.
[51] R. Luo, Relations between landslides induced by wenchuan earthquake and InSAR deformation field and coulomb stress change[D], Southwest Jiaotong University, 2016 [in Chinese].
[52] Y.H. Yang, Fault slip inversion of wenchuan earthquake using InSAR coseismic surface deformation observations[D], Southwest Jiaotong University, 2015 [in Chinese].
[53] Y.M. Wen, C.J. Xu, Z.H. Li, et al., Coseismic and postseismic deformation of the 2008 wenchuan earthquake from InSAR[J], Chin. J. Geophys. 57 (6) (2014) 1814–1824.
[54] C.J. Xu, G.L. Lin, Y.M. Wen, Extract and analysis surface deformation caused by wenchuan Mw7.9 earthquake from InSAR data[J], Geomatics Inf. Sci. Wuhan Univ. 35 (10) (2010) 1138–1142.
[55] Z.H. Li, B.Q. Han, Z.J. Liu, et al., Source parameters and slip distributions of the 2016 and 2022 Menyuan, Qinghai earthquakes constrained by InSAR observations[J], Geomatics Inf. Sci. Wuhan Univ. 47 (6) (2022) 887–897.
[56] R.J. Wang, L.M. Francisco, R. Frank, PSGRN/PSCMP—a new code for calculating Co- and post-seismic Deformation,Geoid and gravity changes based on the viscoelastic-gravitational dislocation theory[J], Comput. Geosci. 32 (4) (2006) 527–541.
[57] R. Zhang, Z.Q. Zhang, D.W. Zheng, et al., Coulomb stress transfer of strong earthquakes within tectonic belts near western Ordos block[J], Chin. J. Geophys. 64 (10) (2021) 3576–3599 [in Chinese].
[58] X.B. Zou, Study on tectonic deformation and seismogenic mechanism of the Minle-Yongchang active fault in the Hexi Corridor[D], Lanzhou Institute of Seismology, 2018 [in Chinese].
[59] L.Y. Ji, Q.L. Wang, J. Xu, C.W. Ji, et al., The july 11, 1995 Myanmar–China earthquake: a representative event in the bookshelf faulting system of southeastern asia observed from JERS-1 SAR images[J], Int. J. Appl. Earth Obs. Geoinf 55 (2017) 43–51, https://doi.org/10.1016/j.jag.2016.10.006.
[60] J. Ye, M. Liu, How Fault evolution changes strain partitioning and fault slip rates in southern California: results from geodynamic modeling[J], J. Geophys. Res. Solid Earth 122 (8) (2017) 6893–6909, https://doi.org/10.1002/2017JB014325.
[61] L.P. Fan, B.R. Li, S.R. Liao, C. Jiang, L.H. Fang, High-precision relocation of the aftershock sequence of the January 8, 2022, MS6.9 Menyuan earthquake, Earthq. Sci. 35 (2) (2022) 138–145, https://doi.org/10.1016/j.eqs.2022.01.021.
[62] J. Liu, Z. Ren, H. Zhang, C. Li, Z. Zhang, W. Zheng, X. Li, C. Liu, Slip rates along the laohushan fault and spatial variation in slip rate along the Haiyuan fault zone, Tectonics 41 (2022) e2021TC006992, https://doi.org/10.1029/2021TC006992.

Qiang Zhao, Master, China Earthquake Administration (CEA), senior engineer of the Second Monitoring and Application Center, CEA. The main research direction is the application of space geodetic technology in seismic monitoring.